ADVANCED MATERIALS
www.advmat.de

Extreme Biomimetics: Designing of the First Nanostructured 3D Spongin–Atacamite Composite and its Application

Dmitry Tsurkan, Paul Simon, Christian Schimpf, Mykhaylo Motylenko, David Rafaja, Friedrich Roth, Dmytro S. Inosov, Anna A. Makarova, Izabela Stepniak, Iaroslav Petrenko, Armin Springer, Enrico Langer, Anton A. Kulbakov, Maxim Avdeev, Artur R. Stefankiewicz, Korbinian Heimler, Olga Kononchuk, Sebastian Hippmann, Doreen Kaiser, Christine Viehweger, Anika Rogoll, Alona Voronkina, Valentine Kovalchuk, Vasilii V. Bazhenov, Roberta Galli, Mehdi Rahimi-Nasrabadi, Serguei L. Molodtsov, Parvaneh Rahimi, Sedigheh Falahi, Yvonne Joseph, Carla Vogt, Denis V. Vyalikh, Martin Bertau, and Hermann Ehrlich**

Dedicated to the memory of Dr. Izabela Stepniak

The design of new composite materials using extreme biomimetics is of crucial importance for bioinspired materials science. Further progress in research and application of these new materials is impossible without understanding the mechanisms of formation, as well as structural features at the molecular and nano-level. It presents a challenge to obtain a holistic understanding of the mechanisms underlying the interaction of organic and inorganic phases under conditions of harsh chemical reactions for biopolymers. Yet, an understanding of these mechanisms can lead to the development of unusual—but functional—hybrid materials. In this work, a key way of designing centimeter-scale macroporous 3D composites, using renewable marine biopolymer spongin and a model industrial solution that simulates the highly toxic copper-containing waste generated in the production of printed circuit boards worldwide, is proposed. A new spongin–atacamite composite material is developed and its structure is confirmed using neutron diffraction, X-ray diffraction, high-resolution transmission electron microscopy/selected-area electron diffraction, X-ray photoelectron spectroscopy, near-edge X-ray absorption fine structure spectroscopy, and electron paramagnetic resonance spectroscopy. The formation mechanism for this material is also proposed. This study provides experimental evidence suggesting multifunctional applicability of the designed composite in the development of 3D constructed sensors, catalysts, and antibacterial filter systems.

1. Introduction

Biomimetics aims at scientifically grounded imitation of natural phenomena, processes, and fascinating architectural principles of natural materials using a whole arsenal of modern tools and ultrahigh-speed computing. The fundamental difference between natural engineering processes and biomimetic engineering lies in their ultimate goals. The biological reason for the biomaterials creation is strictly subordinated to any organism's task of survival benefits due to skeletal structures optimized via evolutionary selection and functionalization. Man, peeping at nature, pursues his technical, technological, and economic goals.

Extreme biomimetics in materials science can be defined as the search for natural biomaterial sources outside the human comfort zone (temperature, toxicity, pH, salinity, pressure, etc.) for engineering inspiration to create inorganic–organic hybrid composites resembling their unique properties.[1] Although these

---

D. Tsurkan, Dr. I. Petrenko, Dr. P. Rahimi, S. Falahi, Prof. Y. Joseph, Prof. H. Ehrlich
Institut of Electronic- und Sensor Materials
TU Bergakademie Freiberg
Gustav-Zeuner-Str. 3, 09599 Freiberg, Germany
E-mail: Hermann.Ehrlich@esm.tu-freiberg.de

The ORCID identification number(s) for the author(s) of this article can be found under https://doi.org/10.1002/adma.202101682.

DOI: 10.1002/adma.202101682

Dr. P. Simon
Max-Planck Institute for Chemical Physics of Solids
Nöthnitzer Str. 40, 01187 Dresden, Germany

Dr. C. Schimpf, Dr. M. Motylenko, Prof. D. Rafaja
Institute of Materials Science
TU Bergakademie Freiberg
09599 Freiberg, Germany

Dr. F. Roth
Institute of Experimental Physics
TU Bergakademie Freiberg
09599 Freiberg, Germany

biomaterials' main components are still the common structural polysaccharides (cellulose, chitin) or structural proteins (collagens, spongin), only a limited number of them, which can be useful in extreme biomimetics, have been found in nature.[2,3] For practical applications, special priority is given to renewable biopolymers, which exclude the deliberate depletion of corresponding natural resources.

Marine keratosan (or bath) sponges, through marine farming, have established themselves as a global renewable source of the unique naturally 3D prefabricated biomaterial spongin, which can reach the size of up to 70 cm in diameter.[1] This microfibrous structural biocomposite possesses complex chemistry from a biomaterials science view. Their skeletal structural motifs match well with artificially designed bio-based porous organic materials (i.e., collagen, silk, chitosan, cellulose)[4–10] as well as with trends recognized for porous scaffolds design.[11,12] Previously, spongin-based templates have been used to produce 3D porous hydroxyapatite ceramics[13,14] including a calcination approach at remarkable 750 °C.[15]

The exact composition of spongin is unknown; it has a collagen-based main structural motif of the proteinaceous origin but contains a significant amount of cysteine and halogenated (I, Br, Cl) amino acid residues. It also has been found to contain xylose[16] and even calcium and silica in picomolar concentrations.[1,17,18] Together, its unique composition is responsible for both mechanical robustness and the exceptional resistance to a wide variety of proteolytic enzymes and acids.[17] As a natural elastomer, spongin is thermally stable up to 300 °C, which motivated researchers to apply spongin as an organic matrix in diverse hydrothermal synthesis reactions using extreme biomimetics routes.[18] Nowadays, this strategy made it possible

---

A. A. Kulbakov, Prof. D. S. Inosov
Institute of Solid State and Materials Physics
TU Dresden
D-01069 Dresden, Germany

A. A. Kulbakov, Prof. D. S. Inosov
Dresden-Würzburg Cluster of Excellence on Complexity and Topology in Quantum Matter (ct.qmat)
TU Dresden
D-01062 Dresden, Germany

Dr. A. A. Makarova
Institute of Chemistry and Biochemistry
Free University of Berlin
D-14195 Berlin, Germany

Dr. I. Stepniak[†]
Institute of Chemistry and Technical Electrochemistry
Poznan University of Technology
ul. Berdychowo 4, Poznan 60-965, Poland

Dr. A. Springer
Medizinische Biologie und Elektronenmikroskopisches Zentrum (EMZ)
Strempelstraße 14, 18057 Rostock, Germany

Dr. A. Springer
Universitätsmedizin Rostock
Strempelstraße 14, 18057 Rostock, Germany

Dr. E. Langer
Institute of Semiconductors and Microsystems
TU Dresden
01062 Dresden, Germany

Dr. M. Avdeev
Australian Nuclear Science and Technology Organisation
New Illawarra Road, Lucas Heights, NSW 2234, Australia

Prof. A. R. Stefankiewicz, Prof. H. Ehrlich
Center for Advanced Technologies
Adam Mickiewicz University
Poznań, Poland

Prof. A. R. Stefankiewicz
Faculty of Chemistry
Adam Mickiewicz University
Poznań, Poland

K. Heimler, C. Viehweger, A. Rogoll, Prof. C. Vogt
Institute of Analytical Chemistry
TU Bergakademie Freiberg
Leipziger Str. 29, 09599 Freiberg, Germany

Dr. O. Kononchuk, Dr. D. Kaiser, Dr. S. Hippmann, Prof. M. Bertau
Institute of Chemical Technology
TU Bergakademie Freiberg
Leipziger Straße 29, 09599 Freiberg, Germany
E-mail: Martin.Bertau@chemie.tu-freiberg.de

[†]Deceased January 2021

Dr. A. Voronkina
Department of Pharmacy
National Pirogov Memorial Medical University
Vinnytsia 21018, Ukraine

Prof. V. Kovalchuk
Department of Microbiology
National Pirogov Memorial Medical University
Vinnytsia 21018, Ukraine

Dr. V. V. Bazhenov, Prof. S. L. Molodtsov
European XFEL GmbH
Holzkoppel 4, 22869 Schenefeld, Germany

Dr. R. Galli
Department of Medical Physics and Biomedical Engineering
Clinical Sensoring and Monitoring – Anesthesiology and Intensive Care Medicine
Faculty of Medicine Carl Gustav Carus
Technische Universität Dresden
Fetscherstraße 74, 01307 Dresden, Germany

Prof. M. Rahimi-Nasrabadi
Chemical Injuries Research Center
Systems Biology and Poisonings Institute
Baqiyatallah University of Medical Sciences
Tehran 1951683759, Iran

Prof. M. Rahimi-Nasrabadi
Faculty of Pharmacy
Baqiyatallah University of Medical Sciences
Tehran 1951683759, Iran

Prof. S. L. Molodtsov
Saint-Petersburg National Research University of Information Technologies
Mechanics and Optics
ITMO University
St. Petersburg 197101, Russia

Prof. D. V. Vyalikh
Donostia International Physics Center (DIPC)
Donostia-San Sebastián 20018, Spain

Prof. D. V. Vyalikh
IKERBASQUE
Basque Foundation for Science
Bilbao 48011, Spain

Prof. H. Ehrlich
Centre for Climate Change Research
Toronto, ON M4P 1J4, Canada

Prof. H. Ehrlich
A.R. Environmental Solutions
ICUBE-University of Toronto Mississauga
Mississauga, ON L5L 1C6, Canada

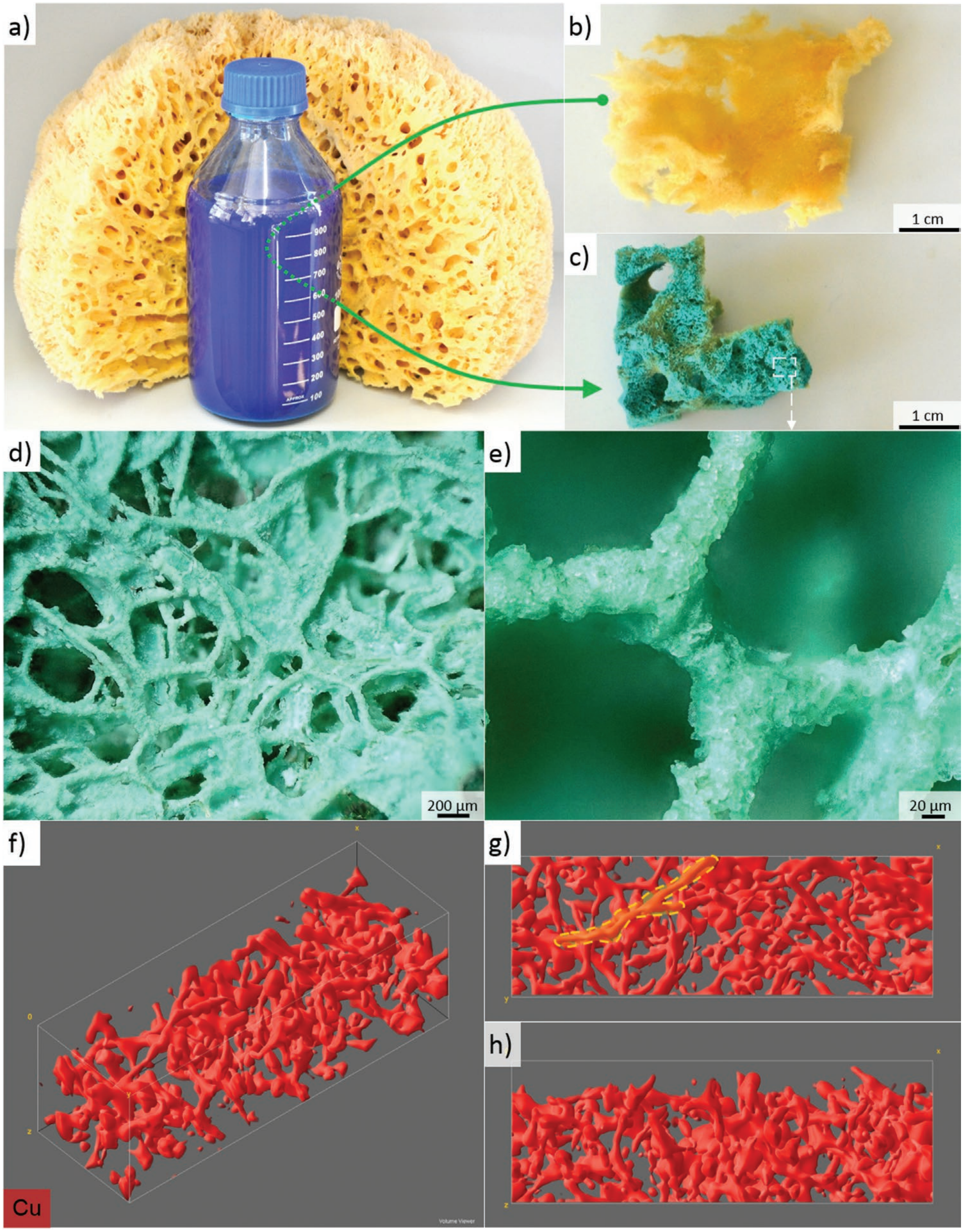

Figure 1. Biological material meets alkaline, toxic Cu-based waste. a–d) A spongin-based porous microfibrous scaffold of *Hippospongia communis* bath sponge with the original 3D architecture, when placed in a model ammoniacal $CuCl_2$ solution (a,b), is covered with a dense layer of green crystalline material (c,d), which has been identified in this study as atacamite. e) The crystalline phase remains firmly attached to the spongin fibers even after 72 hours of ultrasonic treatment at 37 °C (see also Figure S1, Supporting Information). f–h) The 3D distribution of copper in the spongin–atacamite composite, which was measured with a confocal 3D-µXRF setup in sample dimensions of $1.5 \times 0.5 \times 0.5$ mm^3 3D perspective (f), top view (g), side view (h) and the highlighted typical spongin structure unit (yellow marking).

to obtain new hybrid materials based on fibrous spongin and metal oxides such as TiO_2[19] and MnO_2.[20,21] Spongin 3D scaffolds can be carbonized at high temperatures in oxygen-free conditions. Moreover, as reported recently,[1] the preservation of morphological details of spongin scaffolds in the formed graphite has been evidently confirmed even after its carbonization at 1200 °C, which marks a ground-breaking possibility in extreme biomimetics and bioinspired materials science forward.

One of the strategic directions of extreme biomimetics is to study the possibility of using chemically resistant renewable biomaterials for the disposal of highly toxic waste, including metal-containing industrial waste.[22] We focus on the use of spongin and its existing naturally pre-designed 3D architecture that can, in turn, be used in technological processes.

In this work, we have initially created a model industrial solution under laboratory conditions that simulates the highly toxic copper-containing waste generated in the production

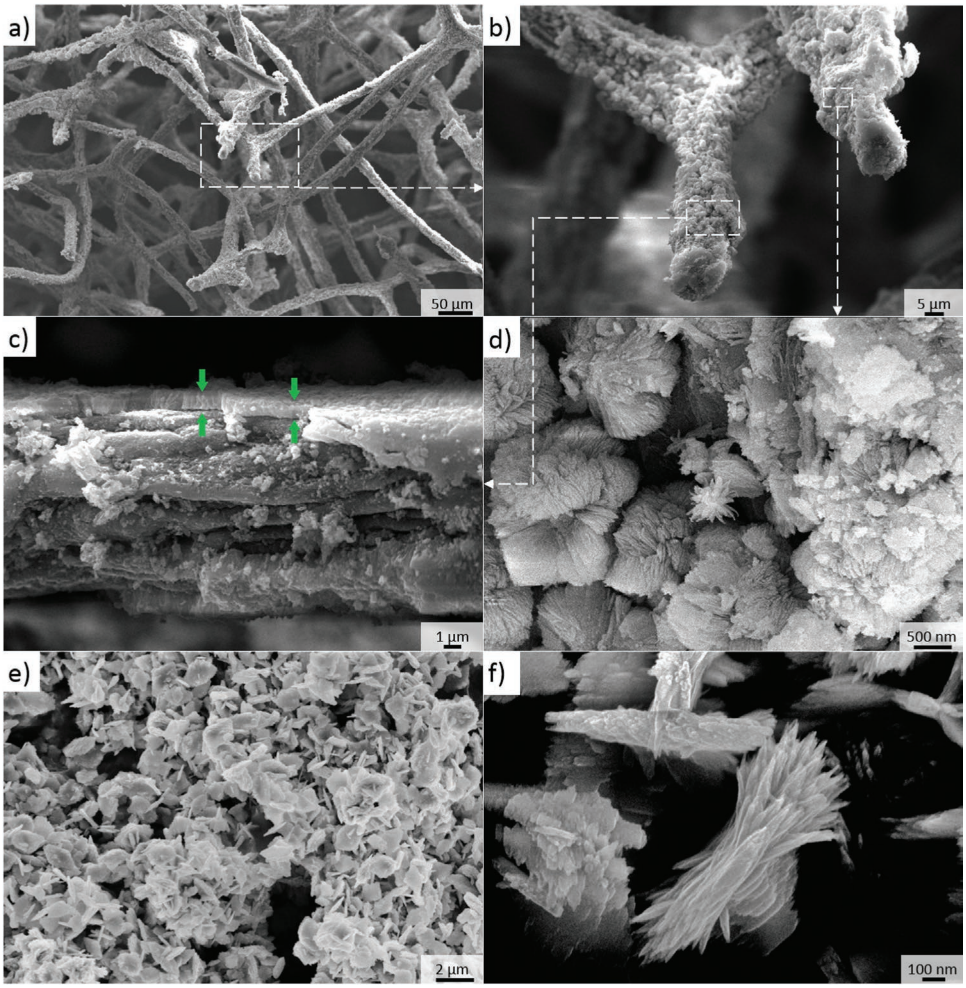

Figure 2. a–d) SEM imaging of the crystalline phase, which remains tightly bound to spongin (see Figure 1e). d) The crystals cover the surface of the microfibers with a 1 ± 0.1 µm thick, dense layer (c, arrows) that contains agglomerated nano- and microcrystalline phases. e) SEM images of residual matter obtained after alkali treatment of 3D spongin–atacamite composite show structural changes. f) Crystalline phase has been identified in this study as CuO (see Figures S2–S6, Supporting Information).

of printed circuit boards using the so-called printing process. Here, up to 70% of the applied copper is removed using an etching solution (ammoniacal $CuCl_2$ solution). During leaching, Cu^{2+} oxidizes the elemental copper on the circuit board to Cu^{+}, and when copper (II) concentration is getting low for effective leaching, the etching solution is exchanged.[23] In the study, we show for the first time that the insertion of ready to use 3D spongin scaffolds into this solution (**Figure 1**) leads to a chemical reaction between the organic template and inorganic ions with the corresponding formation of a new composite material, which contains spongin as organic, and crystalline atacamite ($Cu_2Cl(OH)_3$) as the main inorganic phases. This reaction preserves the macroporous spongin matrix's integrity and obtains a multifunctional macroscopic construct that can be easily regenerated with real prospects for its application for practical purposes at a large scale (Figure S1, Supporting Information).

Atacamite is a rare mineral. Its formation in nature requires saline water,[24] including a reduced environment of hydrothermal sediments in the Red Sea hot brine-filled deeps[25] as well as corrosion of bronze alloys exposed to the marine environment.[26] The only known case of the bio-atacamite identified within animal jaws has been reported for marine Glycera worm.[27] To our best knowledge, the application of copper-chlorides-containing industrial wastewaters as sources for the synthesis of atacamite remains unknown.

2. Results and Discussion

Copper–ammonia waste contains copper in the form of a complex compound—copper (II) tetraamine chloride.[23] Traditionally, for the destruction of this complex compound, for example, hydrochloric acid is needed. However, in our case, the complex collapsed on contact with proteinaceous spongin, followed by the formation of a mineral phase with characteristic crystalline properties (**Figures** 1e and **2**). The crystals remain so firmly attached to the spongin substrate that they do not detach even after 72 hours of sonication at 37 °C (Figures 2b and 4).

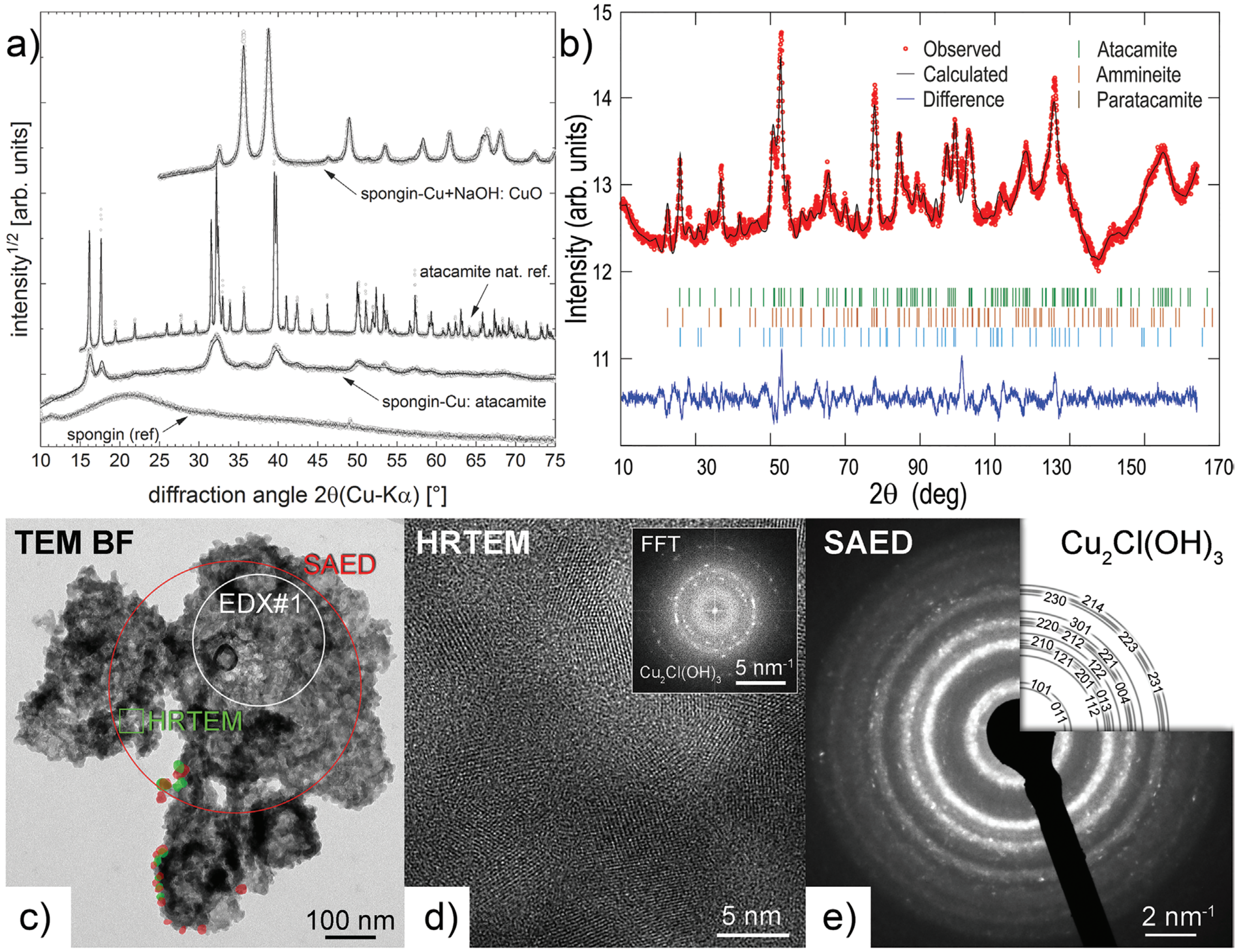

Figure 3. Phase analysis of the spongin–atacamite composite specimen. a) XRD patterns (from bottom to top) of spongin, spongin–atacamite composite, pure natural atacamite reference, and CuO formed after treatment of spongin–atacamite with NaOH are represented in the figure. The open dots represent measured data; the solid represents the results of the Rietveld refinement of the data. The identification of atacamite has also been tested against clinoatacamite having a very similar crystal structure. b) Neutron diffraction data confirmed the presence of atacamite as the main crystalline phase but also ammineite and paratacamite. c–e) TEM bright-field image of the selected spongin–atacamite particle conglomerate with the colored marking of individual nanoparticles (c), as well as areas for HRTEM (d) and SAED (e) analysis. Also, these data unambiguously confirmed the formation of atacamite within the investigated composite material.

Thus, the chemical reaction proceeding at pH 9.1 in the system "reaction solution + spongin" is represented as follows:

$$[\mathrm{Cu(NH_3)_4}]\mathrm{Cl_2} \rightarrow \mathrm{CuCl_2} + 4\mathrm{NH_3} \tag{1}$$

$$4\mathrm{CuCl_2} + 6\mathrm{NH_3} + 6\mathrm{H_2O} \rightarrow 2\mathrm{Cu_2(OH)_3Cl} + 6\mathrm{NH_4Cl} \tag{2}$$

According to our ICP-AES measurements, the obtained atacamite-containing composite powder contains ≈30 ± 4 wt% of copper.

The phenomenon of spongin solubility in alkaline solutions is well known.[17,18] Therefore, we placed a spongin scaffold coated with atacamite (see Figures 1e and 2a,b) in a 10% NaOH solution and kept it there for 48 hours at a temperature of 37 °C. Finally, we observed the collapse of the 3D spongin–atacamite scaffold and the appearance of agglomerated black-colored microcrystals. SEM images of this material (**Figure 3**a,b) show that the agglomerates of micro- and nanocrystals identified by us as tenorite (CuO) (see Figure 3a and Figures S6 and S8, Supporting Information) are still bonded together despite the absence of visible microfibers of spongin. Thus, we suggest the obtaining of spongin–tenorite composite for the first time. However, this material lost 3D architecture that remains to be present in the case of the spongin–atacamite composite. We accept this phenomenon as a disadvantage for practical application at a large-scale level in contrast to robust 3D constructs made of spongin–atacamite material (see Figure 1e,f).

Figure 3a shows the X-ray diffraction (XRD) patterns of individual samples under study. The diffraction pattern of the spongin reference is similar to those, which have been reported earlier.[1] The formation of crystalline atacamite ($Cu_2Cl(OH)_3$)

on the spongin scaffold being in contact with a $CuCl_2$ solution was confirmed by XRD phase analysis and subsequent Rietveld refinement.[28] Atacamite crystallizes in the orthorhombic space group *Pnma* with the lattice parameters a = 6.035 Å, b = 6.872 Å, and c = 9.126 Å (ICDD PDF-4+ database, card no. 01-080-9252).[29] Within the experimental error, the refined lattice parameters (a = (6.033 ± 0.002) Å, b = (6.867 ± 0.004) Å, c = (9.127 ± 0.002) Å) agree with the lattice parameters from the above reference. As can be seen in Figure 3a, the sample does not contain other phases since all observed peaks belong to the atacamite phase. However, we cannot exclude the traces of other atacamite-related phases, such as clinoatacamite (paratacamite)[30] and botallackite,[31] which at low concentrations cannot be detected by XRD.

The size of atacamite crystallites grown on spongin is ≈20 nm. A very high microstrain in the atacamite phase ($\approx 8.5 \times 10^{-3}$) indicates a large number of microstructure defects. Within the frame of this work, the kind of microstructure defects must remain unspecified. The small crystallite size is one of the reasons for the large broadening of the XRD lines. Another factor that contributes to the XRD line broadening is the presence of crystal structure imperfections, which are caused by the growth of atacamite at a low temperature. The effect of the crystal structure defects in the atacamite detected within the spongin–atacamite composite is illustrated by the differences in the XRD patterns of the sample under study and a reference sample of atacamite mineral. The XRD analysis of this reference sample revealed the lattice parameters a = (6.032 ± 0.002) Å, b = (6.868 ± 0.001) Å, and c = (9.121 ± 0.003) Å, which are in agreement with the database entry and with the refined lattice parameters of atacamite found on spongin. However, the XRD lines are much narrower, as the atacamite in the reference sample has much fewer crystal structure defects.

Treatment of the spongin–atacamite composite in a 10% NaOH solution (Figure 2d,e) leads to the transformation of $Cu_2Cl(OH)_3$ to CuO. CuO crystallizes in the monoclinic space group *C2/c* with the lattice parameters a = 4.685 Å, b = 3.426 Å, c = 5.130 Å, and β = 99.55° (ICDD PDF-4+ database, card no. 00-045-0937). The lattice parameters determined using Rietveld refinement were a = (4.683 ± 0.001) Å, b = (3.430 ± 0.002) Å, c = (5.132 ± 0.001) Å, and β = (99.27 ± 0.03)°. The approximate crystallite size is 25 nm. A microstrain parameter of the order of 1.5×10^{-3}, which is a high value but also somewhat lower than for atacamite, indicates a high concentration of defects in the crystal structure of CuO. However, their detailed investigation is beyond the scope of this report. Secondary phases have not been observed in this sample using XRD.

Additionally, for phase identification in the TEM, the characteristic areas on the TEM grid with samples were selected and analyzed using a combination of high-resolution TEM and diffraction. Figure 3c represents a selected fragment of spongin–atacamite composite with $Cu_2Cl(OH)_3$ particles, which have a size of 20–30 nm and form a conglomerate. The size of the individual particles can be seen from the colored highlighting. The high-resolution transmission electron microscopy (HRTEM) image shows, however, that these particles consist of several nanocrystallites with a crystallite size of 5–7 nm (Figure 3d). The calculated FFT (inset) of HRTEM image consists of almost complete circles, which reflects the fine crystallinity of the particles. The analysis of the circle radius shows that these particles can be assigned to the atacamite phase (space group *Pnma*). This is also confirmed by the analysis of selected-area electron diffraction (SAED) pattern (Figure 3e), which was recorded from a larger area of the sample. The diffraction rings are completely closed and broadened as a result of the statistically distributed orientations of crystallite or small crystallite size.

The analysis of the composite obtained after the reaction with NaOH shows the great changes in the microstructure. The individual particles have the shape of plates with fine fibers on the edges (Figure 2f and Figure S6a, Supporting Information). The phase analysis of these plates (Figures S6b,c, Supporting Information) confirms the results of the XRD, namely the formation of monoclinic CuO phase (space group *C2/c*). It can be clearly seen from both HRTEM/FFT and SAED images that these plates are single crystalline. Their size varies considerably and reaches a few micrometers.

The analytical methods (EDX and electron energy loss spectroscopy (EELS)) (see Figure S7, Supporting Information) also confirm the formation of the CuO phase. The comparison of the EDX spectra recorded from corresponding regions of the sample (see Figure 3c and Figure S6a, Supporting Information) before (Figure S7a, Supporting Information) and after (Figure S7d, Supporting Information) the reaction with NaOH clearly shows the disappearance of the Cl K_α peak in the spongin–CuO composite. The analysis of the energy-loss near-edge structure (ELNES) of O K edge also shows great changes after the chemical reaction. While the three characteristic peaks[32,33] in the energy range 530–550 eV are observed in CuO (Figure S7e, Supporting Information), the intensity shifts in the area of peaks 2 and 3 in the atacamite (Figure S7b, Supporting Information) can be clearly seen. In contrast, the changes in ELNES of Cu $L_{2,3}$ edge are minimal and mainly affect the L_2 white line (Figure S7c,f, Supporting Information). The small plateau to the right of the L_2 peak (Figure S7f, Supporting Information) can be regarded as a sign of the presence of a certain portion of Cu(I) in the sample.[32,33]

Furthermore, we have used neutron diffraction as a method that is much more sensitive than XRD to the differences between various polymorphs of atacamite, mainly due to the sensitivity to hydrogen positions and non-decaying form factor. The obtained neutron diffraction pattern of the spongin–atacamite composite is represented in Figure 3b. In the sample under study, atacamite dominates at ≈82%, while the rest is the mineral ammineite, $Cu(NH_3)_2Cl_2$.[34] The only difference between copper–ammonia [$Cu(NH_3)_4Cl_2$] and ammineite [$Cu(NH_3)_2Cl_2$] is the number of ammonia groups. We suggest that it may represent an intermediate phase in the reduction of $Cu(NH_3)_4Cl_2$ to ammonia-free $Cu_2Cl(OH)_3$. The third phase in this sample is paratacamite with negligible 4%.

Additional experiments confirm the presence of an atacamite-spongin composite on the nanoscopic level. As observed in the overview images of the ultramicrotomy (**Figure 4**), the scaffold possesses a central helically twisted spongin-fibril serving as the main skeleton for the spongin shape (Figure 4a,b, yellow arrows). At the spongin surface, the mineralization process occurs, giving rise to ≈1 µm down to nanosized composite aggregates (Figure 4a,b, red arrows) forming the outer shell. Further enlargement reveals the nanofibrous structure

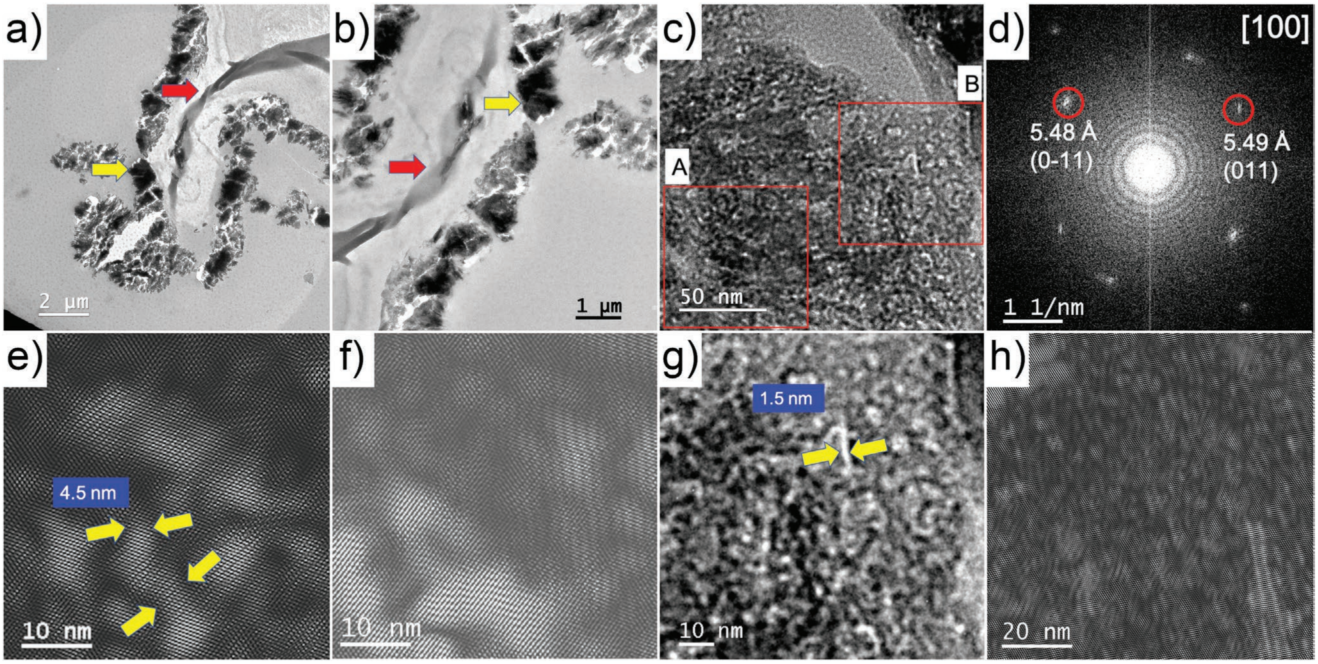

Figure 4. Ultrastructural features of the spongin–atacamite composite. a,b) Overview through the cross-section of the spongin–atacamite microfragments (red arrow). The mineral layer (yellow arrow) fell off the splinter partially from the organic phase when cutting the sample with the microtome. However, selected nanocrystals remain to be localized on the spongin fiber (see zoom (c) into the spongin–atacamite composite). d) FFT of red marked area A in (c) showing (011) and (1–10) reflections of the atacamite lattice indicating [100] zone.[35] e) Fourier filtered image of the enlarged area in the region of interest of rectangle A. Crystal lattice is appearing in the bright areas visible as fine white/black stripes reproducing spongin shape with microfibril-like fine structure with a diameter of ≈4.5 nm (yellow arrows) corresponding to the diameter of collagen fibril in a bundle. f) Another Fourier filtered area of A indicates massive crystallization at the bottom (bright area). g) The filtered area is marked as region B in image (c). Typical for spongin triple-helical fibrils of collagen diameter of ≈1.5 nm[1,36] are well visible (see yellow arrows). h) Same area Fourier filtered image displaying crystal lattice also reflecting spongin structure: Fourier (using Bragg reflections of atacamite) filtering was applied indicating the crystal lattice occurrence at the bright areas (g).

of spongin mineralized by atacamite. In order to reveal the composite structure at the nanoscale, Fourier filtering was performed on region A in (c). Figure 4e,f show filtered images of different regions within A. The spongin fibril pattern is superimposed by the atacamite crystal lattice observed as fine bright/dark stripes.

We believe that, by analogy with biominerals, the organic phase should be preserved inside the crystals of atacamite. This suggestion has been confirmed using FTIR and Raman spectroscopy (see Figures S5 and S8, respectively, Supporting Information).

Soft X-ray spectroscopy techniques are particularly well suited to monitor electronic and chemical states of matter with the elemental site-specificity and chemical sensitivity that is required to test and improve our fundamental understanding of interfacial chemistry in complex systems. **Figure 5**a shows a comparison between survey spectra of the spongin reference, atacamite reference, the spongin–atacamite composite as well as the spongin–tenorite composite measured with a photon energy of 1486.68 eV (Al K_{α}). These wide energy spectra reflect all elements present at the sample surface and allow subsequent acquisition of X-ray photoelectron spectroscopy (XPS) fingerprints of the elements, as discussed in detail below.

As expected, the spongin reference sample spectrum is dominated by core-level excitations originating from carbon, nitrogen, oxygen, and calcium. Additionally, at lower binding energies, two peaks that can be attributed to Si (Si 2p and Si 2s) can be observed. The observation of contributions from calcium and silicon at the picomolar level has also been reported previously.[1] The core-level photoemission peaks dominate the survey spectrum of the atacamite reference sample originate from copper (e.g., Cu 3p at 82 eV, Cu 3s at 124 eV, and Cu 2p at 934.6 eV) as well as the corresponding Auger peaks in the 570–725 eV range. Interestingly, the elemental composition of the spongin–atacamite composite is very similar to the survey spectra of the atacamite reference sample (especially chlorine can be found in both spectra) that confirms the formation of atacamite crystals at the surface of the spongin skeleton after the treatment with the Cu-based waste (Figure 1). Moreover, the handling with sodium hydroxide in the case of the spongin–tenorite composite is reflected by the observation of the Na 1s core-level signal. No core-level peaks related to chlorine and silicon can be found after the NaOH treatment.

To obtain a more detailed picture of the oxidation state of copper, we focused on the high-resolution spectra of the Cu-derived core-level signals. Figure 5b shows a comparison between the Cu 2p excitations for the atacamite reference, spongin–atacamite composite, and spongin–tenorite composite. The signal of all three samples is characterized by the typical two spin-orbit components (Cu $2p_{1/2}$ and Cu $2p_{3/2}$), separated in energy by 20 eV. The overall shape of the observed spectra is similar to results published in the literature for related

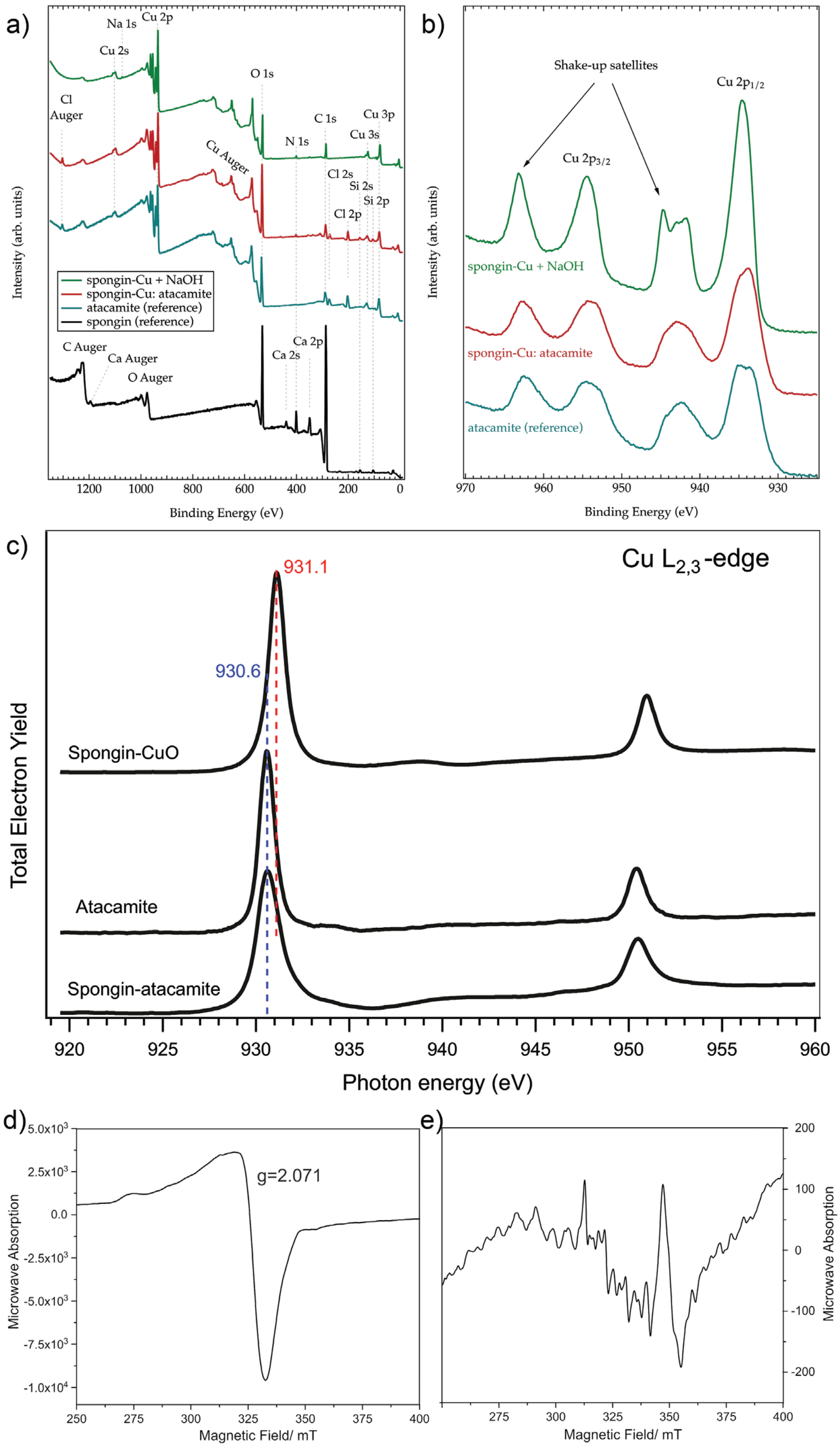

Figure 5. a) Survey XPS spectra of the spongin reference (black line), atacamite reference (blue line), spongin–atacamite composite (red line), and spongin–tenorite composite (green line). b) Comparison between the high-resolution Cu 2p core-level spectra of the atacamite reference (blue), spongin–atacamite composite (red), and spongin–CuO composite. c) NEXAFS spectra at Cu $L_{2,3}$-edge for the spongin–CuO, spongin–atacamite biocomposite, and atacamite standard. The narrow peak at ≈931 eV indicates the presence of $3d^9$ character in the ground state. Therefore, NEXAFS at Cu $L_{2,3}$-edge confirms the Cu^{2+} oxidation state for all the samples. d,e) EPR spectra at room temperature of the spongin–atacamite composite powder (d) and the atacamite standard powder (e).

compounds.[37–39] Moreover, the Cu 2p signal is also characterized by intense shake-up satellites (Figure 5b), which can be seen as direct evidence that Cu(II) compounds are the majority constituents at the surface of the samples[40,41] and confirms the XRD results described above. However, in the case of the atacamite reference sample as well as the spongin–atacamite composite, we observe a double peak structure for the Cu $2p_{1/2}$ core-level, which can be explained by a mixture of Cu(I) and Cu(II) components. Further on, by comparing the spectra of the spongin which was placed in the $CuCl_2$ solution (Figure 5b, red curve) with the Cu 2p spectrum of the atacamite reference sample (Figure 5b, blue curve) no fundamental differences in shape, as well as energy position of the peaks, can be observed. This finding confirms the hypothesis that atacamite crystals are grown on the surface of the spongin template. After the treatment of the spongin–atacamite composite with NaOH we observe a small shift of the Cu $2p_{1/2}$ XPS line to higher binding energies, the disappearance of the double peak as well as a narrowing of the core-level features. This can be explained by the collapse of the spongin–atacamite scaffold and the transformation to CuO. Furthermore, the formation of Cu(II) carbonate dihydroxides could also be a reason for the observed changes in the spectrum. This is supported by characteristic features for metal carbonates and metal hydroxides in the O 1s core-level spectrum (not shown).

It is well recognized that near-edge X-ray absorption fine structure (NEXAFS) spectroscopy allows gaining further insight into the chemical state of copper.[42] In Figure 5c we show the NEXAFS spectra taken from the studied composites together with the reference object atacamite. The narrow peak seen at ≈931 eV is a clear indication of the Cu $3d^9$ configuration in the ground state. Thus, the NEXAFS spectrum taken at Cu $L_{2,3}$-edge unambiguously confirms the Cu^{2+} oxidation state for all samples. Obviously, the NEXAFS spectra (Figure 5c) from spongin–atacamite composite and atacamite standard fit nicely to each other, while there is a well-seen shift of 0.5 eV between the Cu L_3-spectral lines for two biocomposites: spongin–CuO (tenorite) and spongin–atacamite. This is linked with the different crystal field stabilization or hybridization in the ground state.[42] It is worth noting that the peaks' spectral shape and positions are in good agreement with the reference data obtained by van der Laan et al. in 1992 for the variety of copper minerals.[42]

Electron paramagnetic resonance (EPR) spectroscopy is a powerful technique to receive information about paramagnetic species (unpaired electrons) in materials. The EPR spectrum of the spongin–atacamite composite powder shows an intensive peak with a g factor of 2.071 (Figure 5d). This EPR signal corresponds to Cu(II) ions in a tetragonally distorted environment in an octahedral complex in comparison to the literature.[43,44] Also, a small hyperfine splitting of Cu(II) (nuclear spin: 3/2) is allusively shown at lower magnetic fields (275–300 mT). The atacamite did not induce the EPR signal because its EPR spectrum looks quite different (Figure 5e). In these crystals, Cu(II) is arranged in a distorted rhombic environment.[43] The EPR signal of the spongin–atacamite composite indicates a type-1 copper–protein complex.[45,46] The reduced hyperfine coupling (Figure 5d) could be a sign of covalent Cu—S bonds in the composite material.[47] Moreover, the structural refinement of neutron diffraction data of the spongin–atacamite composite from this study indicates the existence of further crystalline phases, especially ammineite ($CuCl_2(NH_3)_2$) (see also Figure 3b).[34] The EPR signal could also be caused by this mineral or other copper ammonia complexes. The existence of Cu(II) ions might also be the reason for the antibacterial behavior of the spongin–atacamite composite in the antibacterial filtrate experiments (see Figures S12–S18, Supporting Information).

What about the possible mechanism of spongin–atacamite composite formation under harsh for biopolymers reaction conditions approved in our study? Previous literature reports have shown that spongin fibers contain various amino acid sequences, including cysteine, tyrosine, histidine, or lysine.[17,18] The presence of the latter makes the surface of the spongin endowed with structurally distinct functional groups (e.g., SH, OH, NH_2, COOH) that are well-known to efficiently bind to transition metal ions such as Cu(II).[48,49] Such an amino acid-directed ligation process to metal ion usually results in the stabilization of specific peptide structures and overall supramolecular assembly. These phenomena may also explain the generation of highly robust spongin–atacamite composite material wherein multiple coordination interactions between available ligands localized, among others, at the external surface of the spongin and copper ions cause high stability of this assembly even after elongated sonication at elevated temperature. The composition of this material, as well as the oxidation state of the copper ions, have been determined by us using qualitative XRD and neutron diffraction as well as XPS and EPR spectroscopies, which confirmed the dominating role of the atacamite phase (≈82%) and copper oxidation state, respectively (see above). Furthermore, the reduced hyperfine coupling observed in the EPR spectra (see Figure 5d) was assigned to the covalent Cu—S bonds, thus confirming the stabilizing role of the amino acid side chains (cysteine) of the spongin. The structural features and composition of spongin–atacamite composite material are changed significantly under alkaline conditions (pH ≈ 9) in which thiol groups of the cysteines are converted into thiolate anions (RS-), which, in the presence of cupric ions (play oxidative catalytic role) formed initially Cys–Cu(I) complex followed by its oxidation to cystine (as a result, the collapse of 3D spongin–atacamite scaffold is observed as confirmed by XPS analysis).

To be sure that SH groups in spongin remain crucial in forming the spongin–atacamite composite, we carried out comparative experiments under the same reaction conditions with fibrous collagen and cellulose. As represented in Figure S9, Supporting Information, any kind of atacamite crystal formation has been observed on these substrates, which originally lack SH groups. As an outcome of this experiment, it can be hypothesized here that keratin can probably be used as an industrial waste substrate for the development of similar atacamite-based composites. However, there are no 3D porous constructs in size (70+ cm) and shape similar to ready-to-use naturally pre-designed spongin scaffolds of marine sponges origin to our best knowledge.

Perspectives of practical applications of 3D functional composite materials, especially at a large scale, remain challenging topics in modern bioinspired materials science and biomimetics.[50] In this study, we deal with the unique situation when both structure and physicochemical features of renewable, naturally prestructured 3D macroscaffolds of biological origin open the key to creating new composite materials by effective utilization of toxic industrial copper-containing wastes. Below, we represent experimentally approved examples (i.e., sensors, catalysts, and filters with antibacterial properties) with respect to outlook how and where designed in this study composite material could be used.

The development of reliable, fast, and cheap enzyme-free biosensing platforms for the detection of glucose is of considerable importance. Recently, there is a great amount of interest in designing enzyme-less electrochemical sensing assays based on various biocompatible metal nanostructures and their oxides as catalysts for the electro-oxidation of glucose. Non-enzymatic glucose sensors overcome the drawbacks of enzymatic glucose sensors like poor stability/reproducibility, degradation of enzyme activity, complicated immobilization process, and high cost.[51,52]

Herein, for the first time, a new enzyme-free sensor for the direct sensing of glucose based on using of spongin–atacamite composite (A-Sp) as a biocompatible catalyst was fabricated and electrochemically characterized. In order to compare the performance of modified carbon paste electrode (CPE) with A-Sp composite, a bare CPE and a CPE modified with standard atacamite (A-St) powder were fabricated. **Figure 6**a presents the cyclic voltammograms (CVs) of different electrodes in 0.1 м NaOH solution in the absence and presence of 0.4×10^{-3} м glucose. As seen, there is no obvious signal response in the absence of glucose for all of the prepared electrodes. The addition of glucose has no influence on the bare CPE, but A-Sp/CPE and A-St/CPE exhibited a remarkably improved current response for glucose oxidation. The enhanced electrocatalytic performance of A-Sp/CPE compared to that of A-St/CPE may be attributed to the 3D spongin–atacamite scaffold, which provides a large surface area and good crystalline structure, thus helping the fast diffusion of glucose molecules in the 3D network and fast electron transfer between glucose and atacamite. Figure 6b displays the electrocatalytic response of A-Sp/CPE for a successive addition of glucose in 0.1 м NaOH. It can be seen that the oxidation peak current was linearly increased over the wide concentration range of 0.1×10^{-3} м to 10.8×10^{-3} м with a slope of 12.46 µA mм$^{-1}$ (sensitivity) and a correlation coefficient of 0.9974. The detection limit of the electrode was found to be 23×10^{-6} м at a signal-to-noise ratio of 3. The modified electrode shows high stability in detection of glucose and preserves 95% of its initial current after 50 cycles in a certain concentration of glucose.

What about spongin–atacamite composite as a catalyst?

Due to its thermal stability of over 300 °C, the composite is an interesting alternative to conventional catalysts. Copper catalysts already have a wide range of industry and research applications (e.g., methanol production and oxidation). In most cases, it is copper oxide on solid supports, which is reduced to elemental copper shortly before the reaction. The elemental copper is then the active center for catalysis. A similar procedure is conceivable with the 3D spongin–atacamite composite (see Figure S10, Supporting Information). By reduction in nitrogen and/or hydrogen stream, the copper species contained are reduced to elemental copper, generating elemental copper as the active species. However, copper(II) oxide (CuO) can also be used for heterogeneous catalysis. One example is the partial catalytic oxidation of methanol to formaldehyde. The metal oxide deposited on a porous support material with a high specific surface area should improve the activity of the catalyst and thus the yield of formaldehyde. Since the combination of sponge fibers and atacamite is a promising precursor for the preparation of a supported CuO catalyst, the application of thermally pre-treated spongin–atacamite composite for the production of formaldehyde was investigated for the first time. The use of this material in a fixed bed reactor demonstrated that it could catalyze the partial oxidation of methanol

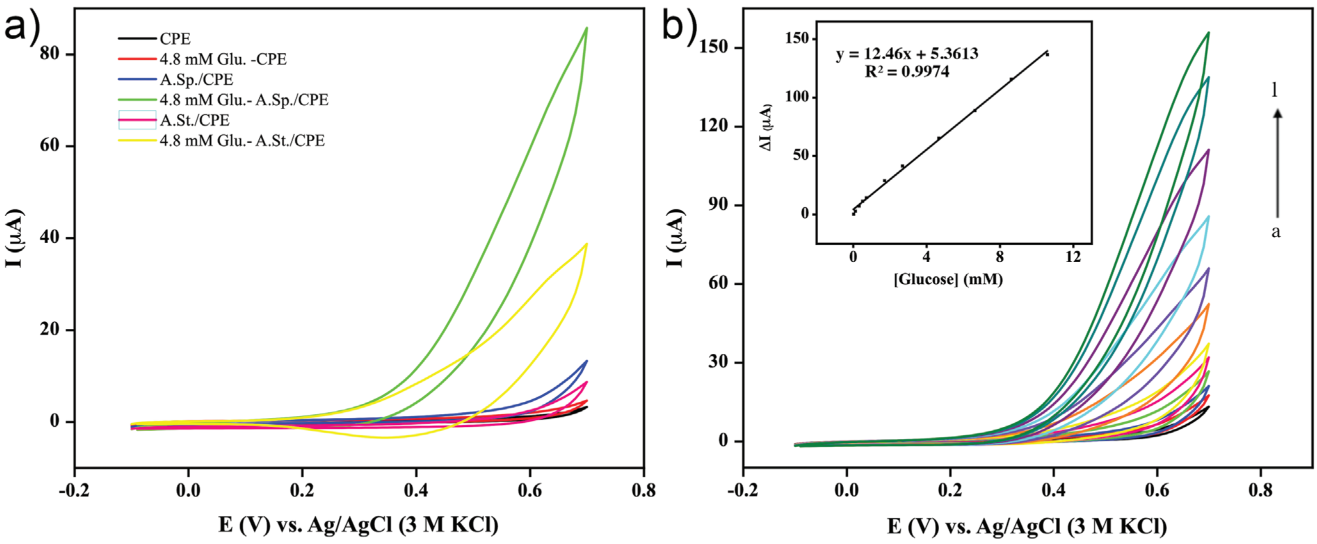

Figure 6. a) CV of CPE, A.Sp./CPE, and A.St./CPE in N_2-saturated 0.1 м NaOH solution in the absence and presence of 4.8×10^{-3} м glucose at a scan rate of 0.1 V s^{-1}. b) The CV of A.Sp./CPE in N_2-saturated 0.1×10^{-3} м NaOH solution containing various glucose concentrations from a to l (0 to 10.8×10^{-3} м) at a scan rate of 0.1 V s^{-1}. Insert: Corresponding calibration between glucose concentration and current density.

to formaldehyde. In a temperature range of 285–300 °C, the formaldehyde yield in the first laboratory tests reached 4–6% (Figure S10, Supporting Information). Although this is still far from a technically relevant yield (>80%), it shows that the material is catalytically active and represents a promising starting material for heterogeneous catalysis.

In a few cases, copper salts are used as catalysts, too. For example, $CuCl_2$ is applied as a co-catalyst in the Wacker-process or for the oxidation of phenols. In this case, it is a homogeneous catalyst. Associated with this are the problems that the catalyst cannot be recovered at all or only with great effort and can thus be reused. In addition, this is associated with complex wastewater treatment, which significantly increases the process costs. Therefore, alternatives are being sought which make it possible to convert the homogeneous catalyst into a heterogeneous one. The spongin–atacamite composite is a promising alternative, which allows for combining Cu(II)-species with a solid carrier. Exploratory experiments have been promising here. We could show that is possible to use the spongin–atacamite composite for the production of furfural from xylose as well as the oxidation of lignin (see Figure S11, Supporting Information). As these are two important processes in the context of biorefineries, this opens up a field of application that will play a decisive role in the future in the area of defossilization of the economy.

We suggest that spongin–atacamite composite in the form of centimeter-large scaffolds (see Figure S1, Supporting Information) could be used as antibacterial filter systems. It is well known that copper-ammonium in solutions that range between 1.4[53] and 3000 ppm[54] is enough to eliminate 100% of bacteria such as *Escherichia coli* that is a strong indicator of sewage or animal waste contamination in water. Similar results have also been obtained in our experiments with *E. coli* ATCC 25 922 strain, where the growth of this bacteria has been completely inhibited due to the application of filtrates from spongin–atacamite composite with a copper content of ≈4 ppm (ICP-AES data).

With regard to the usage of spongin in a recycling process, it was important to prove the renewability of the spongin scaffolds after immersion in a copper–ammonium waste solution. Corresponding experiments have been carried out by us (see Figure S15 and Table S1, Supporting Information). With the aim to obtain mineral-free spongin, selected fragments of spongin–atacamite composite have been treated with 2 wt% nitric acid in an ultrasonic bath for 2 min, cleaned with high purity water, and dried at 80 °C for 2 h. The purified spongin scaffolds have been used again in the reaction, which leads to the formation of atacamite as described above. Now, the way to optimize this procedure as well as to approve the limits of spongin renewability is open.

What about 3D printing of spongin, which can potentially enhance the absorption capacity of this biopolymer due to a surface area increase? Although proteins are particularly appealing to formulate inks for 3D printing,[55] spongin remains to be an exceptional case. In contrast to collagen,[56,57] silk,[58,59] or keratin,[60] 3D printing of spongin at this moment is only hypothetical. The main change in this development is the non-homogenous chemical composition of spongin, which does not rely on an individual, chemically pure, structural protein. We believe that the development of an appropriate spongin formulation seems to be a difficult but very intriguing task for independent, future research.

3. Conclusion

Extreme biomimetics is the search for natural sources of engineering inspiration well outside the human comfort zone (temperature, toxicity, pH, salinity, pressure, etc.). Our strategy for generating new spongin-based composites, using an extreme biomimetic approach, aims at developing high-performance 3D structural composites with enhanced multifunctional capabilities. The goal is to achieve essential improvements in integrity, performance, testability, robustness, reliability, and cost-effectiveness, allowing further applications. Here, we have developed an atacamite-containing composite in the form of already existing macroporous bioarchitecture. The resulting material resembles the size and shape of a cultivated marine sponge. The use of natural polymers to substitute those of artificial origin offers a strategic and viable method to produce 3D material scaffolds. For example, as we have shown, the biopolymer spongin has specific physicochemical properties enabling the fabrication of atacamite-bearing composite using highly toxic copper-rich industrial waste. Moreover, the ability of such a biomaterial to regenerate after chemical removal of the mineral phase is extremely attractive for industrial purposes. Thus, the aim is to design a bridge between extreme biomimetics and bioinspired materials science, where the basic principle is to exploit chemically and thermally stable, renewable biopolymers for the development of the next generation of biologically inspired composite materials. Many of these materials have never been reported or even suggested before and have properties to allow their large-scale application at the extreme conditions of modern industrial processes.

4. Experimental Section

Materials: Copper (II) chloride dihydrate, ammonium carbonate, ammonium chloride and 25% ammonia solution were purchased from Riedel–de Haën AG, Th. Geyer GmbH & Co. KG and abcr GmbH, Germany, in analytical grade quality. All reagents were used as received without further purification. A model copper–ammonia etching solution ($[Cu(NH_3)_4]Cl_2$ solution; 60 wt% Cu) was prepared as described previously.[61] Purified spongin scaffolds of *H. communis* marine demospoge, porcine collagen standard and cellulose standard from *Luffa aegiptica* plant have been purchased from INTIB GmbH (Freiberg, Germany). The atacamite mineral standard was found in 1910 in Chuquicamata district, Chile. This unique sample was kindly provided by the Mineralogical Collection of the TU Bergakademie Freiberg, Germany.

Preparation of Model Copper–Ammonia Waste: 110 g of ammonium chloride, 70 g copper (II) chloride dihydrate, 22 g of ammonium carbonate, and 220 mL of ammonia were dissolved in distilled water in a 1 L measuring flask. 30 g of Cu chips had been etched using this solution for 4 hours. The etching process was carried out at pH 9.1 and a constant stirring rate of 240 rpm and 50 °C using a magnetic stirrer with a heating function. After 4 hours, copper chips were dissolved. The resulting solution was cooled down to room temperature and used for further experiments. Analysis of the model copper-ammonium waste (copper concentration determination) was carried out by employing optical emission spectrometry using inductively coupled plasma-optical emission spectrometer ICP-OES OPTIMA 4300 DV of Perkin Elmer Inc. (USA).

Preparation of Spongin–Atacamite Composite: The purified samples of spongin scaffolds were immersed in a model copper-ammonium waste solution and in distilled water (control sample). Both samples were fixed with the tooling made of surgical steel. The incubation time was 48 hours. The samples were then extracted from the solutions, rinsed in dist. water, and dried in an oven at 80 °C, and, on request, ground in liquid nitrogen using mortar with pestle.

Analytical Techniques: ICP-AES Analysis: iCAP 6000 spectrometer (Thermo Fisher Scientific Inc.); rf power: 1200 W, axial viewing plasma mode (Cu 223.008 nm; Cu 224.700 nm; Cu 327.396 nm; coolant gas flow: 14 L min^{-1}; auxiliary gas flow: 0.6 L min^{-1} nebulizer gas flow: 0.6 L min^{-1}).

Tubes were ultrasonic pre cleaned with 2% nitric acid and high purity water. The used nitric acid was sub-boiled and the high purity water was purified to 0.055 µS at 20 °C. The copper content of the composite was determined by eight measurements (3 with 1–2 mg composite powder and 5 with ≈5 mg) plus three blank measurements. The copper content of the leaching solution was determined by triple determination plus one blank.

EPR Spectroscopy: The EPR analyses were performed on a MiniScope MS 5000 EPR spectrometer (Freiberg Instruments, Germany). The powder samples were measured with 30.0 mW microwave power in borosilicate tubes. A magnetic field range from 250.0 to 400.0 mT, a modulation of 0.9 mT and a sweep time of 60 s were used. The software ESRStudio 1.21.8 was taken for measurement and determination of the *g* factor.

Microscopy: The samples were observed and analyzed with the use of an advanced imaging and measurement system consisting of a VHX-6000 (Keyence, Osaka, Japan) digital optical microscope and VH-Z20R swing-head zoom lenses (magnification up to 200×).

SEM/EDX: SEM images were observed using a Hitachi S-4700 II equipped with a cold field-emission gun. The energy-dispersive X-ray spectroscopy (EDS) was carried out at 20 kV on a JEOL scanning electron microscope JSM-6610LV (LaB_6 filament) at a working distance of 10.0 mm with an Bruker XFlash 6|10 silicon drift detector (SDD, detector area of 10 mm^2) with an energy resolution of 123.8 eV at Mn-K-alpha and the detector window AP3.3.

HR-TEM/SAED: The microstructure characterization of the composites on a microscopic level was carried out using TEM JEM-2200FS. The morphology of the samples was analyzed using imaging, spectroscopic and diffraction methods. The phase composition was mainly determined with the analysis of SAED and fast Fourier transforms (FFTs) of local areas of the HRTEM images. The analytical methods of TEM, namely EDS and EELS, were used for the chemical analysis. HRTEM and SAED images as well as the EELS spectra were recorded using a highly sensitive 2k × 2k CCD camera from Gatan. The EDX spectra were recorded with the help of JED-2300 detector from Jeol with an energy resolution of 130 eV and evaluated with the “Analysis Station” software package. EELS spectra were recorded with an energy resolution of 1 eV using a CCD camera. The DigitalMicrograph program from Gatan was used to analyze the ELNES. TEM samples were prepared by sedimentation of the powder particles of the composite on the TEM gold grid.

Additionally, TEM was carried out on a FEI Tecnai F30-G2 with Super-Twin lens (ThermoFischer, Eindhoven, The Netherlands) with a field emission gun at an acceleration voltage of 300 kV. The point resolution amounts to 2.0 Å, and the information limit to ≈1.2 Å. The microscope is equipped with a wide-angle slow scan CCD camera (MultiScan, 2k × 2k pixels; Gatan Inc., Pleasanton, CA, USA).

XPS: XPS analyses were performed using an ESCALAB 250Xi spectrometer from ThermoFisher Scientific. The system is equipped with a monochromatic Al K_α X-ray source ($h\nu = 1486.68$ eV), operating at a high voltage of 15 kV and focused to a spot size of 500 µm. The base pressure of the analysis chamber was in the mid 10^{-10} mbar range. Survey spectra were recorded with a pass energy of 100 eV, whereas the high-resolution core-level spectra were obtained using a pass energy of 20 eV. A flood electron gun was used for charge compensation.

NEXAFS: These measurements were performed at the Russian–German dipole beamline (RGBL-dipole) of the synchrotron light source BESSY II (Helmholtz-Zentrum, Berlin). NEXAFS spectra were recorded in total-electron yield mode. All measurements were performed at room temperature.

XRD: The identification of crystalline phases and the refinement of the lattice parameters were done using XRD in conjunction with the Rietveld full profile analysis.[28] XRD patterns were recorded with a Seifert/FPM RD7 diffractometer equipped with a sealed X-ray tube with Cu anode. The experiment was performed in symmetrical Bragg–Brentano diffraction geometry. The powder sample was put on a zero-background holder (Si, <510> cut). The diffracted beam passed a set of slits and a graphite monochromator before being detected by a proportional counter.

Neutron Diffraction: Neutron powder diffraction data were collected on the high-resolution powder diffractometer[62] at the OPAL research reactor, ANSTO, Australia. Polycrystalline samples were loaded into 9 mm diameter cylindrical vanadium cans and the measurements were carried out at room temperature using neutrons of the wavelength $\lambda = 2.4395$ Å. The data were analyzed using the FullProf Suite.[63]

3D-µXRF: The 3D-µXRF analysis was performed on a modified M4 TORNADO µXRF spectrometer (Bruker Nano GmbH, Berlin, Germany).[64] The spectrometer was equipped with a 30 W Rh-Tube (metal-ceramic micro focus tube), operated at high-voltage of 50 kV and an anode current of 600 µA. The commercial µXRF setup was equipped with a polycapillary lens with a spot size ≤ 20 µm (Mo K_α) for X-ray focusing and a 30 mm^2 SDD. Due to the modification a second polycapillary lens was installed perpendicular to the first one in front of a 60 mm^2 SDD. The composite sample was analyzed by measuring 51 *xy*-mappings inside a volume of $1.5 \times 0.5 \times 0.5$ mm^3. Each mapping was measured with a spot distance of 10 µm, a spot measuring time of 20 ms and five measuring cycles resulting in a total measuring time of 28 min. In view of the integrity of the sample and the analysis of elements with a high fluorescence radiation energy no vacuum was applied to the sample chamber.

The produced 2D datasets consisting of three dimensions, location coordinates *x*, *y*, and the signal intensity, were exported and converted into RGB color coded images via Spyder Software. The stacking of the individual elemental distribution images was carried out with an image editing program (ImageJ). With the plugin Volume Viewer the 2D information of the stacking was converted into a 3D image. The Volume Viewer plugin was used with an image sampling number of 5.0, a tricubric smooth interpolation for visualization and the RGB color space.

Additional data on analytical techniques (FTIR, Raman, fluorescence), preparation of sensors, catalysts as well antibacterial tests are to be found in the Supporting Information.

Supporting Information

Supporting Information is available from the Wiley Online Library or from the author.

Acknowledgements

This work was partially supported by DFG Project HE 394/3, Alexander von Humboldt Foundation (Germany, Georg Forster research fellowship for experienced researchers program), SMWK Project no. 02010311 (Germany), Polish National Agency for Academic Exchange (NAWA) Ulam International Programme PPN/ULM/2020/1/00177; by Alexander von Humboldt Polish Honorary Research Scholarship (FNP, Poland), OPUS19 (NCN Poland); MAESTRO 12 (NCN Poland). D.S.I. and A.A.K. acknowledge support from DFG within the Würzburg-Dresden Cluster of Excellence ct.qmat (EXC 2147, project-id 390858490). The authors thank H. Meissner, E. Bailey, A. L. Stelling, K. Tabachnik, J. Beyer, and J. Heitmann for helpful discussions.

Open access funding enabled and organized by Projekt DEAL.

Note: Parvaneh Rahimi and Sedigheh Falahi had been declared as authors of this work in the cover letter accompanying the submission, but their names were omitted in the manuscript itself for publication. The two names were added to the published author list on July 26, 2021, after initial publication online. P.R. and S.F. designed and performed the experiments for sensing of glucose based on using of spongin–atacamite composite. P.R. wrote up that section (Enzyme-Free Biosensing) in the Experimental Section of the article. In addition to this, the spelling of the name Valentine Kovalchuk was corrected, a fourth affiliation for Prof. Hermann Ehrlich was added (Centre for Climate Change Research Toronto), the department name with which Prof. Valentine Kovalchuk is affiliated at National Pirogov Memorial Medical University was corrected to the Department of Microbiology, which meant the addition of a further numbered affiliation was required, and the author list for the current affiliation 23 (Saint-Petersburg National Research University of Information Technologies) was revised.

Conflict of interest

The authors declare no conflict of interest.

Data Availability Statement

Research data are not shared.

Keywords

atacamite, catalysts, composites, extreme biomimetics, sensors, spongin, tenorite

Received: March 1, 2021
Revised: April 27, 2021
Published online: June 3, 2021

---

[1] I. Petrenko, A. P. Summers, P. Simon, S. Żółtowska-Aksamitowska, M. Motylenko, C. Schimpf, D. Rafaja, F. Roth, K. Kummer, E. Brendler, O. Pokrovsky, R. Galli, M. Wysokowski, H. Meissner, E. Niederschlag, Y. Joseph, S. Molodtsov, A. Ereskovsky, V. Sivkov, S. Nekipelov, O. Petrova, O. Volkova, M. Bertau, M. Kraft, A. Rogalev, M. Kopani, T. Jesionowski, H. Ehrlich, *Sci. Adv.* **2019**, *5*, eaax2805.
[2] D. Tsurkan, M. Wysokowski, I. Petrenko, A. Voronkina, Y. Khrunyk, A. Fursov, H. Ehrlich, *Appl. Phys. A* **2020**, *126*, 382.
[3] H. Ehrlich, *Int. Geol. Rev.* **2010**, *52*, 661.
[4] Q. Zhang, S. Yan, M. Li, *Materials* **2009**, *2*, 2276.
[5] U. G. T. M. Sampath, Y. C. Ching, C. H. Chuah, J. J. Sabariah, P. C. Lin, *Materials* **2016**, *9*, 991.
[6] S. Ling, D. L. Kaplan, M. J. Buehler, *Nat. Rev. Mater.* **2018**, *3*, 18016.
[7] I. R. Lednev, K. V. Apryatina, L. A. Smirnova, *Key Eng. Mater.* **2019**, *816*, 214.
[8] D. Lopez-Barrerio, Z. Martin-Moldes, J. Yeo, S. Shen, M. J. Hawker, F. J. Martin-Martinez, D. L. Kaplan, M. J. Buehler, *Adv. Mater.* **2019**, *31*, 1904720.
[9] C. Li, C. Guo, V. Fitzpatrick, A. Ibrahim, M. J. Zwierstra, P. Hanna, A. Lechtig, A. Nazarian, S. J. Lin, D. L. Kaplan, *Nat. Rev. Mater.* **2020**, *5*, 61.
[10] M. S. B. Reddy, D. Ponnamma, R. Choudhary, K. K. Sadasivuni, *Polymers* **2021**, *13*, 1105.
[11] J. Ren, Y. Wang, Y. Yao, Y. Wang, X. Fei, P. Qi, S. Lin, D. L. Kaplan, M. J. Buehler, S. Ling, *Chem. Rev.* **2019**, *119*, 12279.
[12] T. Liu, G. Liu, *Nat. Commun.* **2020**, *11*, 4984.
[13] E. Cunningham, N. Dunne, G. Walker, C. Maggs, R. Wilcox, F. Buchanan, *J. Mater. Sci.: Mater. Med.* **2010**, *21*, 2255.
[14] S. A. Clarke, S. Y. Choi, M. McKechnie, G. Burke, N. Dunne, G. Walker, E. Cunningham, F. Buchanan, *J. Mater. Sci.: Mater. Med.* **2016**, *27*, 2016.
[15] A. A. Barros, I. M. Aroso, T. H. Silva, J. F. Mano, A. R. Duarte, R. L. Reis, *Biomed. Mater.* **2016**, *11*, 045004.
[16] S. Teckmann, N. Öner, *Nature* **1963**, *200*, 77.
[17] H. Ehrlich, M. Wysokowski, S. Żółtowska-Aksamitowska, I. Petrenko, T. Jesionowski, *Mar. Drugs* **2018**, *16*, 79.
[18] T. Jesionowski, M. Norman, S. Żółtowska-Aksamitowska, I. Petrenko, Y. Yoseph, H. Ehrlich, *Mar. Drugs* **2018**, *16*, 88.
[19] T. Szatkowski, M. Wysokowski, G. Lota, D. Peziak, V. V. Bazhenov, G. Nowaczyk, J. Walter, S. L. Molodtsov, H. Stöcker, C. Himcinschi, I. Petrenko, A. L. Stelling, S. Jurga, T. Jesionowski, H. Ehrlich, *RSC Adv.* **2015**, *5*, 79031.
[20] *Extreme Biomimetics*, (Ed.: H. Ehrlich), Springer International Publishing, Cham, Switzerland **2017**.
[21] T. Szatkowski, K. Kopczyński, M. Motylenko, H. Borrmann, B. Mania, M. Graś, G. Lota, V. V. Bazhenov, D. Rafaja, F. Roth, J. Weise, E. Langer, M. Wysokowski, S. Żółtowska-Aksamitowska, I. Petrenko, S. L. Molodtsov, J. Hubálková, C. G. Aneziris, Y. Joseph, A. L. Stelling, H. Ehrlich, T. Jesionowski, *Nano Res.* **2018**, *11*, 4199.
[22] E. M. Domingues, G. Gonçalves, B. Henriques, E. Pereira, P. A. A. P. Marques, *J. Hazard. Mater.* **2021**, *407*, 124807.
[23] O. O. Kononchuk, S. Hippmann, M. Bertau, A. I. Alexeev, *Chem. Ing. Tech.* **2020**, *92*, 368.
[24] M. D. Hannington, *Can. Mineral.* **1993**, *31*, 945.
[25] D. J. Mossman, K. J. Heffernan, *Chem. Geol.* **1978**, *21*, 151.
[26] L. Gianni, *Ph.D. Thesis*, Ghent University (Ghent, Belgium) and Sapienza University of Rome (Rome, Italy), **2011**.
[27] H. C. Lichtenegger, T. Schöberl, M. H. Bartl, H. Waite, G. D. Stucky, *Science* **2002**, *298*, 389.
[28] *The Rietveld Method*, International Union of Crystallography, (Ed.: R. A. Young), Oxford University Press, Oxford, UK **1995**.
[29] B. P. Onac, H. S. Effenberger, N. C. Collins, J. B. Kearns, R. C. Breban, *Int. J. Speleol.* **2011**, *40*, 99.
[30] M. E. Fleet, *Acta Crystallogr., Sect. B: Struct. Sci., Cryst. Eng. Mater.* **1975**, *B31*, 183.
[31] F. C. Hawthorne, *Mineral. Mag.* **1985**, *49*, 87.
[32] O. Heckl, F. Haider, J. Gegner, *Int. J. Mater. Res.* **2008**, *99*, 496.
[33] Y. Wang, S. Lany, J. Ghanbaja, Y. Fagot-Revurat, Y. P. Chen, F. Soldera, D. Horwat, F. Mücklich, F. Pierson, *Phys. Rev. B* **2016**, *94*, 245418.
[34] H.-P. Bojar, F. Walter, J. Baumgartner, G. Färber, *Can. Mineral.* **2010**, *48*, 1359.
[35] J. B. Parise, B. G. Hyde, *Acta Crystallogr., Sect. C: Struct. Chem.* **1986**, *C42*, 1277.
[36] P. Simon, D. Grüner, H. Worch, W. Pompe, H. Lichte, T. El Khassawna, C. Heiss, S. Wenisch, R. Kniep, *Sci. Rep.* **2018**, *8*, 13696.
[37] M. C. Squarcialupi, G. P. Bernardini, V. Faso, A. Atrei, G. Rovida, *J. Cult. Heritage* **2002**, *3*, 199.
[38] A. Mezzi, E. Angelini, T. De Caro, S. Grassini, F. Faraldi, C. Riccucci, G. M. Ingo, *Surf. Interface Anal.* **2012**, *44*, 968.
[39] V. Hayez, A. Franquet, A. Hubin, H. Terryn, *Surf. Interface Anal.* **2004**, *36*, 876.
[40] M. C. Biesinger, *Surf. Interface Anal.* **2017**, *49*, 1325.
[41] C. C. Chusuei, M. A. Brookshier, D. W. Goodman, *Langmuir* **1999**, *15*, 2806.
[42] G. van der Laan, R. A. D. Pattrick, C. M. B. Henderson, D. J. Vaughan, *J. Phys. Chem. Solids* **1992**, *53*, 1185.
[43] S. L. Reddy, T. Endo, *Trans. Mater. Res. Soc. Jpn.* **2010**, *35*, 423.
[44] S. Hashimoto, H. Takeda, S. Honda, Y. Iwamoto, *Constr. Build. Mater.* **2015**, *88*, 143.

[45] R. Guzzi, A. Stirpe, M. P. Verbeet, L. Sportelli, *Eur. Biophys. J.* **2001**, *30*, 171.
[46] M. Flores, T. L. Olson, D. Wang, S. Edwardraja, S. Shinde, J. C. Williams, G. Ghirlanda, J. P. Allen, *J. Phys. Chem. B* **2015**, *119*, 13825.
[47] E. I. Solomon, R. G. Hadt, *Coord. Chem. Rev.* **2011**, *255*, 774.
[48] S. Mandal, G. Das, R. Singh, R. Shukla, P. K. Bharadwaj, *Coord. Chem. Rev.* **1997**, *160*, 191.
[49] H. Kozłowski, T. Kowalik-Jankowska, M. Jeżowska-Bojczuk, *Coord. Chem. Rev.* **2005**, *249*, 2323.
[50] Y. Khrunyk, S. Lach, I. Petrenko, H. Ehrlich, *Mar. Drugs* **2020**, *18*, 589.
[51] A. K. Mishra, D. K. Jarwal, B. Mukherjee, A. Kumar, S. Ratan, M. R. Tripathy, S. Jit, *Sci. Rep.* **2020**, *10*, 11451.
[52] L. Wang, S. Jia, N. Wang, X. Cao, *Int. J. Nanomanuf.* **2016**, *12*, 298.
[53] Q. Qin, J. Li, J. Wang, *Water Environ. Res.* **2017**, *89*, 378.
[54] T. A. Danilova, G. A. Danilina, A. A. Adzhieva, E. I. Vostrova, V. G. Zhukhovitskii, S. B. Cheknev, *Bull. Exp. Biol. Med.* **2020**, *169*, 648.
[55] X. Mu, F. Agostinacchio, N. Xiang, Y. Pei, Y. Khan, C. Guo, P. Cebe, A. Motta, D. L. Kaplan, *Prog. Polym. Sci.* **2021**, *115*, 101375.
[56] G. Grezzana, H.-C. Loh, Z. Qin, M. J. Buehler, A. Masic, F. Libonati, *Adv. Eng. Mater.* **2020**, *22*, 2000387.
[57] W. W. Chan, D. C. L. Yeo, V. Tan, S. Singh, D. Choudhury, M. W. Naing, *Bioengineering* **2020**, *7*, 66.
[58] X. Mu, V. Fitzpatrick, D. L. Kaplan, *Adv. Healthcare Mater.* **2020**, *9*, 1901552.
[59] X. Mu, J. K. Sahoo, P. Cebe, D. L. Kaplan, *Polymers* **2020**, *12*, 2936.
[60] J. K. Placone, J. Navarro, G. W. Laslo, M. J. Lerman, A. R. Gabard, G. J. Herendeen, E. E. Falco, S. Tomblyn, L. Burnett, J. P. Fisher, *Ann. Biomed. Eng.* **2017**, *45*, 237.
[61] O. Kononchuk, S. Hippmann, M. Bertau, A. I. Alexeev, *Chem. Ing. Tech.* **2020**, *92*, 368.
[62] M. Avdeev, J. R. Hester, *J. Appl. Crystallogr.* **2018**, *51*, 1597.
[63] J. Rodríguez-Carvajal, *Phys. B* **1993**, *192*, 55.
[64] I. Mantouvalou, T. Wolf, C. Seim, V. Stoytschew, W. Malzer, B. Kanngießer, *Anal. Chem.* **2014**, *86*, 9774.